

# CHEMISTRY

## A European Journal

A Journal of



### Accepted Article

**Title:** Activating Inert Alkali Metal Ions by Electron Transfer from Manganese Oxide for Formaldehyde Abatement

**Authors:** Jiayi Gao, Zhiwei Huang, Yaxin Chen, Jing Wan, Xiao Gu, Zhen Ma, Jianmin Chen, and Xingfu Tang

This manuscript has been accepted after peer review and appears as an Accepted Article online prior to editing, proofing, and formal publication of the final Version of Record (VoR). This work is currently citable by using the Digital Object Identifier (DOI) given below. The VoR will be published online in Early View as soon as possible and may be different to this Accepted Article as a result of editing. Readers should obtain the VoR from the journal website shown below when it is published to ensure accuracy of information. The authors are responsible for the content of this Accepted Article.

**To be cited as:** *Chem. Eur. J.* 10.1002/chem.201704398

**Link to VoR:** <http://dx.doi.org/10.1002/chem.201704398>

Supported by  
**ACES**

WILEY-VCH

# Activating Inert Alkali Metal Ions by Electron Transfer from Manganese Oxide for Formaldehyde Abatement

Jiayi Gao,<sup>[a]</sup> Zhiwei Huang,<sup>[a]</sup> Yaxin Chen,<sup>[a]</sup> Jing Wan,<sup>[b]</sup> Xiao Gu,<sup>[b]</sup> Zhen Ma,<sup>[a]</sup> Jianmin Chen,<sup>[a]</sup> and Xingfu Tang<sup>\*[a, c]</sup>

**Abstract:** Alkali metal ions often act as promoters rather than active components due to their stable outermost electronic configurations and their inert properties in heterogeneous catalysis. Herein, we activate inert alkali metal ions such as  $K^+$  and  $Rb^+$  by electron transfer from hollandite-type manganese oxide (HMO) support for HCHO oxidation. Results from synchrotron X-ray diffraction, absorption, and photoelectron spectroscopies demonstrate that the electronic density of states of single alkali metal adatoms is much higher than that of  $K^+$  or  $Rb^+$ , because electrons transfer from manganese to the alkali metal adatoms through bridging lattice oxygen. The electron transfer originates from the interactions of alkali  $d$ - $sp$  frontier orbitals with lattice oxygen  $sp^3$  orbitals occupied by lone-pair electrons. Reaction kinetics data of HCHO oxidation reveal that the high electronic density of states of single alkali metal adatoms is favorable for the activation of molecular oxygen. Mn  $L_3$ -edge and O  $K$ -edge soft-X-ray absorption spectra demonstrate that lattice oxygen gains part of electrons from the Mn  $e_g$  orbitals, leading to the upshift of lattice oxygen orbitals in energy. Therefore, the facile activation of molecular oxygen by the electron-abundant alkali metal adatoms and active lattice oxygen are responsible for the high catalytic activity in complete oxidation of HCHO. This work could assist the design of efficient and cheap catalysts by tuning the electronic states of active components.

## Introduction

HCHO has been widely used in making building and furnishing materials, consumer products, etc. The worldwide production capacity for HCHO is over 30 million tons per year.<sup>[1]</sup> However, HCHO emitted from the above materials may cause indoor air

pollution,<sup>[2]</sup> because it can lead to eye, nose, throat, and skin irritation.<sup>[3]</sup> More seriously, long-term exposure to HCHO may lead to cancer.<sup>[4,5]</sup> HCHO has been classified as a probable human carcinogen by the Environmental Protection Agency of USA<sup>[6]</sup> and the World Health Organization.<sup>[3]</sup> Furthermore, HCHO is also one of the typical atmospheric pollutants in the outdoor air,<sup>[7]</sup> because it induces photochemical pollution.<sup>[8,9]</sup> Therefore, it is of vital importance to control the HCHO emission.

Catalytic oxidation of HCHO to  $CO_2$  and  $H_2O$  by using solid catalysts in the presence of molecular oxygen is a promising technology.<sup>[10]</sup> Supported noble metal catalysts often show excellent catalytic performance,<sup>[11–13]</sup> but they are rather expensive. Some transition metal oxides can show catalytic activity as high as noble metal catalysts.<sup>[14,15]</sup> In particular, hollandite-type manganese oxides (HMO) have high catalytic activity in HCHO oxidation because the tunnel sizes are suitable for the adsorption and activation of HCHO<sup>[16]</sup> and for the activation of oxygen<sup>[17]</sup>. To further enhance the catalytic performance, noble metals such as Pt,<sup>[18]</sup> Au,<sup>[19]</sup> and Ag<sup>[20–22]</sup> were highly dispersed or even atomically dispersed/deposited onto HMO surfaces. However, noble metal catalysts can only be applied in some special environments such as aircrafts due to cost reasons.

Occasionally, alkali metals and alkaline earth metals such as  $K^+$  and  $Ca^{2+}$ , atomically dispersed and with high electron density of states, have been proved to be highly active for catalytic oxidation of HCHO.<sup>[23,24]</sup> For instance, Han *et al.* found that isolated  $Ca^{2+}$  in the tunnels of hydroxyapatite showed high catalytic activity in the complete oxidation of HCHO because  $Ca^{2+}$  can activate molecular oxygen.<sup>[24]</sup> Our recent work also showed that single  $K^+$  of a single-site catalyst with hybridized  $d$ - $sp$  orbitals has high electronic density of states and possesses excellent ability towards activating both molecular oxygen and lattice oxygen, and thus the catalyst showed high catalytic activity for HCHO oxidation.<sup>[23]</sup> It should be mentioned that previous studies have found that potassium exhibited promotion effects in Fisher-Tropsch reaction<sup>[25]</sup> and ammonia synthesis,<sup>[26]</sup> and the promoting function of potassium mainly originates from the electron-donating effects of potassium. Likewise, electron-abundant alkalis can facilitate the dissociation of  $O_2$  by charge transfer from potassium to the antibonding orbitals of  $O_2$ , thus showing significant activity in oxidation reactions.<sup>[27–29]</sup>

In this work, a series of alkali metal ions were atomically dispersed on HMO surfaces, and the catalytic performance of these catalysts in HCHO oxidation were studied at low temperatures. The crystal structures and morphologies of the catalysts were determined by using synchrotron X-ray diffraction (SXRD) and transition electron microscopy (TEM). The specific surface areas and pore volumes of the catalysts were analyzed by  $N_2$  adsorption-desorption measurements, and calculated by

[a] J. Gao, Dr. Z. Huang, Dr. Y. Chen, Prof. Z. Ma, Prof. J. Chen, Prof. X. Tang

Institute of Atmospheric Sciences, Shanghai Key Laboratory of Atmospheric Particle Pollution & Prevention (LAP<sup>3</sup>)  
Department of Environmental Science & Engineering  
Fudan University  
200433 Shanghai (P. R. China)  
E-mail: tangxf@fudan.edu.cn

[b] J. Wan, Prof. X. Gu  
Department of Applied Physics  
Chongqing University  
400044 Chongqing (P.R.China)

[c] Prof. X. Tang  
Jiangsu Collaborative Innovation Center of Atmospheric Environment & Equipment Technology (CICAET)  
Nanjing University of Information Science & Technology  
210044 Nanjing (P. R. China)

Supporting information for this article is available on the WWW under <http://dx.doi.org/10.1002/chem.2017xxxx>.

the Brunauer-Emmett-Teller (BET) and the  $t$ -plot method, respectively. The local structures of single alkali adatoms were determined by extended X-ray absorption fine structure (EXAFS) spectra. A combination of X-ray photoelectron spectra (XPS) and X-ray absorption near-edge structure (XANES) spectra revealed the electronic states and the outermost orbital configuration of the isolated alkali ions. Electronic interactions between Mn and O orbitals were also studied by Mn  $L_3$ -edge and O  $K$ -edge soft-X-ray absorption spectra. The catalytic performance of catalysts in HCHO oxidation is correlated with the catalysts' structures and characteristics mainly in terms of the activation of molecular oxygen and active lattice oxygen. This work could open an avenue to develop efficient and inexpensive single-atom catalysts for abating volatile organic compounds such as HCHO.

## Results and Discussion

The SXRD patterns of the samples are shown in Figure 1. Rietveld refinement analyses were performed to investigate the effect of alkalis' loading on HMO. The corresponding lattice parameters and partial atom coordinates are listed in Tables S1 and S2, respectively, from which the structural model can be constructed (Figure 1, insets). HMO can be indexed to a tetragonal structure with an  $I4/m$  space group (Figure S1), and thus HMO, constructed by  $MnO_6$  octahedra, has one-dimensional square tunnels of  $\sim 4.7 \text{ \AA} \times 4.7 \text{ \AA}$  along the  $[001]$  direction. The tunnel walls consist of lattice oxygen with  $sp^3$  hybridization, and these lattice oxygen ions use three  $sp^3$  orbitals to bond to three  $Mn^{4+}$ , and another  $sp^3$  orbital occupied by lone-pair electrons can donate electrons to unoccupied orbitals of anchored metals such as Ag and  $K^+$ .<sup>[23,30,31]</sup>

After loading alkalis, the tetragonal structures are preserved regardless of the types of alkalis, consistent with the results in our recent report.<sup>[32]</sup> One K or Rb ion coordinates to eight O  $sp^3$  orbitals to form bulk-centered tetragonal prism structures according to the Rietveld refinement analyses, and the reconstructed models are shown in the insets of Figure 1. The K-O and Rb-O bond lengths are  $\sim 2.88$  and  $\sim 2.96 \text{ \AA}$ , respectively, equal to the sum of the corresponding ionic radius of alkali ions and lattice oxygen.<sup>[30]</sup> The  $MnO_6$  octahedra are also preserved after loading K or Rb. In Table S1, the lattice parameter  $a$  slightly increases with the atomic number of alkalis, and the lattice parameter  $c$  almost remains unchanged. Thus, the cell volume also increases when these alkali ions are loaded, consistent with the insertion of alkalis into the HMO tunnels in the interval stacking model because of Coulomb charge repulsion.<sup>[31]</sup> Furthermore, the specific surface areas of HMO and alkali-doped HMO are in a range of  $54\text{--}64 \text{ m}^2 \text{ g}^{-1}$ , and the pore volumes calculated from the  $t$ -plot method are about  $1.4\text{--}2.4 \times 10^{-3} \text{ cm}^3 \text{ g}^{-1}$ , as listed in Table S3.

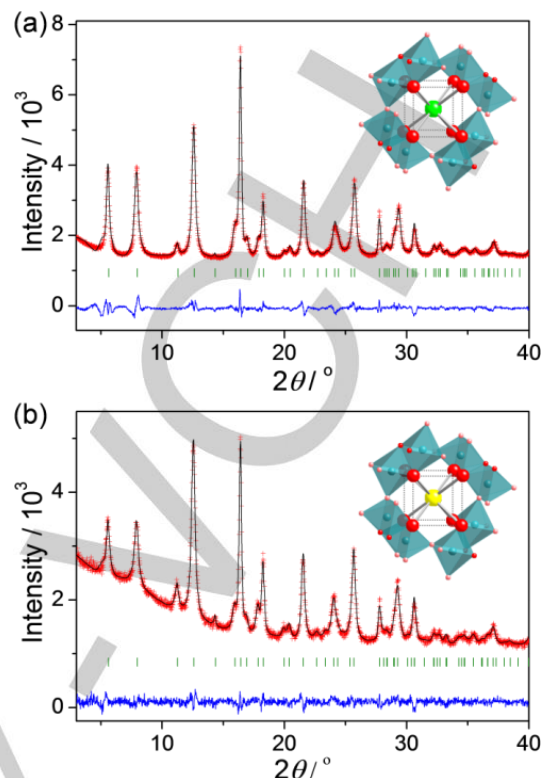


**Figure 1.** SXRD patterns of (a)  $K_1/HMO$  and (b)  $Rb_1/HMO$  including the Rietveld refinements. The blue curves are the differential SXRD patterns. The short vertical lines below the SXRD patterns mark the peak positions of all of the possible Bragg reflections. Insets: oblique perspective models showing alkali ions at the Wyckoff  $2b$  sites. Red, blue, green, and yellow balls represent O, Mn, K, and Rb atoms, respectively, and blue octahedron represents  $MnO_6$ .

The local structures of the alkali atoms were investigated by EXAFS, and the related spectra at the  $K$ -edge are shown in Figure 2. Tables S4 and S5 summarize the structural parameters obtained by fitting the spectra with theoretical models,<sup>[31]</sup> and Figures S2 and S3 illustrate the curve-fitting of  $R$ -space and inverse Fourier transform (FT) spectra. The FT amplitudes of the EXAFS data of  $K_1/HMO$  and  $Rb_1/HMO$  are similar to each other. The results indicate that the immediate structures of K and Rb are almost the same, i.e., they are both located at the Wyckoff  $2b$  sites. The first shells of  $K_1/HMO$  and  $Rb_1/HMO$  are assigned to the A-O bonds with an average bond length of  $\sim 2.88$  and  $2.96 \text{ \AA}$ , respectively, and a coordination number of 8. Thus, a coordination configuration of an  $AO_8$  polyhedron is a  $D_{4h}$  symmetry (Figure 2, insets), as evidenced by the SXRD refinements. The result agrees with the conclusion from the SXRD refinement analyses that the alkali ions are arranged at an alternate stacking model along the HMO tunnel direction. Thus, the alkali ions are located at isolated states and the single alkali metal ions are exposed on the HMO tunnel openings to form "single-atom" alkali catalysts.<sup>[23]</sup> Furthermore, the EXAFS data of the single-atom alkali catalysts are distinctly different from those of KCl and RbOH. The EXAFS spectrum of KCl reveals that the local structure of  $K^+$  is a  $KCl_6$  octahedron with an average K-Cl bond length of  $\sim 3.13 \text{ \AA}$  and an octahedral

( $O_h$ ) symmetry (Figure 2a, inset).<sup>[33]</sup> The EXAFS spectrum of RbOH reveals that the local structure of  $Rb^+$  is a  $RbO_5$  tetragonal pyramid with an average Rb-O bond length of  $\sim 3.02$  Å and a  $C_{4v}$  symmetry (Figure 2b, inset).<sup>[34]</sup>

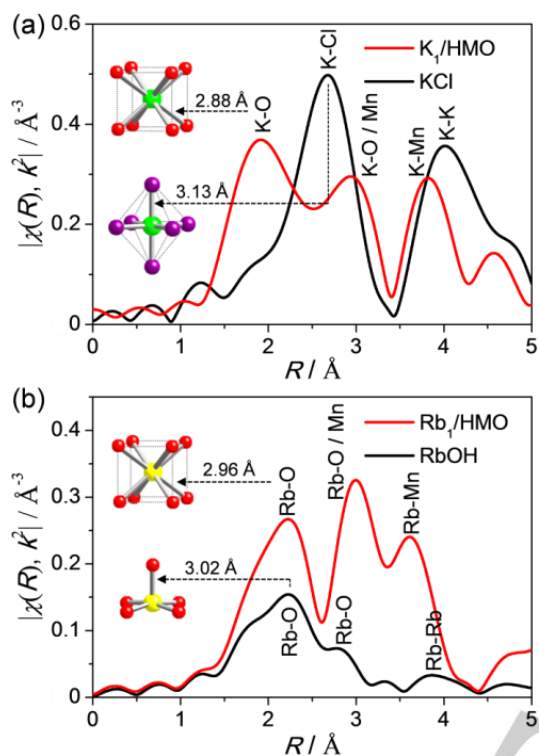


**Figure 2.** FT EXAFS spectra of (a)  $K_1/HMO$  and (b)  $Rb_1/HMO$  at the K and Rb K-edge with the  $k^2$  weight. Red, green, purple, and yellow balls represent O, K, Cl, and Rb atoms, respectively.

The morphologies of HMO,  $K_1/HMO$ , and  $Rb_1/HMO$  were observed by using TEM. As shown in Figure 3, HMO has a rod-shaped morphology with an average length of  $\sim 800$  nm and a width of  $\sim 14$  nm.<sup>[32]</sup> The HMO rods grow along the [001] axis according to the high resolution TEM (HRTEM) image: (i) the fringe distances of 3.26 and 2.4 Å can be assigned to the lattice spacing of the (300) and (211) planes of HMO, respectively, and the (300) plane is parallel to the side line; (ii) A cross angle between the (211) plane and the side line is  $\sim 60^\circ$ . After loading alkalis, the one-dimensional morphologies of HMO remain unchanged. The appearance of smooth surfaces in the TEM images indicates the absence of KCl and RbOH nanoparticles on HMO surfaces, while the presence of K and Rb species is confirmed by energy dispersive X-ray spectrometer (EDX) mapping data. The K/Mn or Rb/Mn molar ratios obtained from EDX determine the formula of  $K_{0.9}Mn_8O_{16}$  and  $Rb_{1.0}Mn_8O_{16}$ , in line with the results obtained by X-ray Fluorescence Spectrometer (XRF) analyses. Consequently, the HMO tunnels are filled with the alkali ions, and alkali ions are exposed on the HMO(001) planes, as modelled in insets of Figure 3d,f.<sup>[23]</sup> These

single alkali metal ions are anchored on oxygen cavity sites consisting of four surface  $sp^3$  oxygen ions.

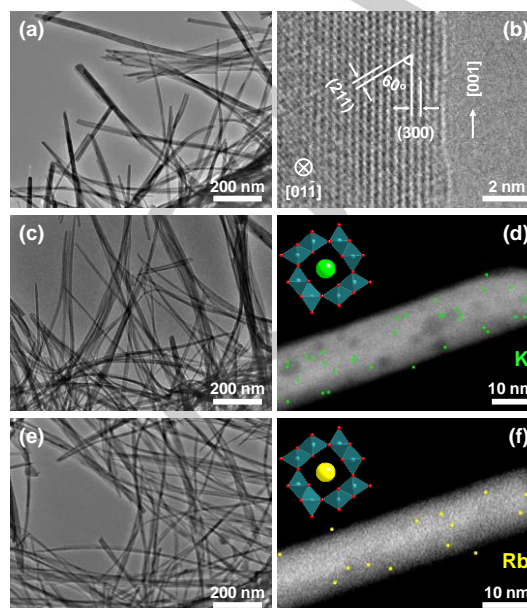


**Figure 3.** TEM images of (a) HMO, (c)  $K_1/HMO$ , and (e)  $Rb_1/HMO$ . (b) HRTEM image of HMO. STEM images, EDX mapping data, and atomic arrangements on the HMO(001) planes of (d)  $K_1/HMO$  and (f)  $Rb_1/HMO$ . Red, blue, green, and yellow balls represent O, Mn, K, and Rb atoms, respectively. Blue octahedron stands for the  $MnO_8$  structural motif.

HMO keeps the same morphology and similar structure after loading alkalis onto it, which is advantageous for comparatively studying the catalytic activity of HMO and the single-atom alkali catalysts. Catalytic oxidation of HCHO was conducted over HMO and the single-atom alkali catalysts at low temperatures, and the results in term of HCHO conversions ( $X_{HCHO}$ ) and  $CO_2$  selectivity as a function of reaction temperature are shown in Figure 4a. All catalysts show 100%  $CO_2$  selectivity at the whole tested temperature window. The  $X_{HCHO}$  over HMO are significantly lower than that over the single-atom alkali catalysts.  $K_1/HMO$  is slightly more active than  $Rb_1/HMO$ , and  $Rb_1/HMO$  is the same active as  $Na_1/HMO$  prepared using a similar method (Figure S4). Over 95%  $X_{HCHO}$  are obtained on these single-atom alkali catalysts at 110 °C, whereas HMO only gives 20%  $X_{HCHO}$  at 110 °C. The single-atom alkali catalysts can even exhibit significant catalytic activities below 90 °C, but HMO is almost not active below 90 °C, implying that the single alkali metal ions anchoring on HMO surfaces serve as catalytically active sites for the low-temperature oxidation of HCHO. Similar results using alkalis as catalytic sites were also reported in the oxidation of soot and volatile organic compounds.<sup>[35,36]</sup>

The apparent activation energy ( $E_a$ ) over  $K_1/HMO$  or  $Rb_1/HMO$  is  $\sim 84$  kJ mol<sup>-1</sup> in HCHO oxidation, approximately 5 kJ mol<sup>-1</sup> lower than that of HMO (Figure 4b). Moreover, when  $Rb^+$  in the form of RbOH was supported on  $TiO_2$ , RbOH/ $TiO_2$  is inactive to HCHO oxidation (Figure S4). Considering the decrease of  $E_a$  after alkali loadings and the inert alkali ions when loaded on  $TiO_2$ ,

it is convincing that the catalytic performance of the single alkali adatoms on HMO is triggered by the interactions among alkalis and HMO.

alkali ions are very active for activating O<sub>2</sub>. Therefore, the single-atom alkali catalysts have significantly strong abilities for activating both molecular O<sub>2</sub> and surface lattice oxygen.

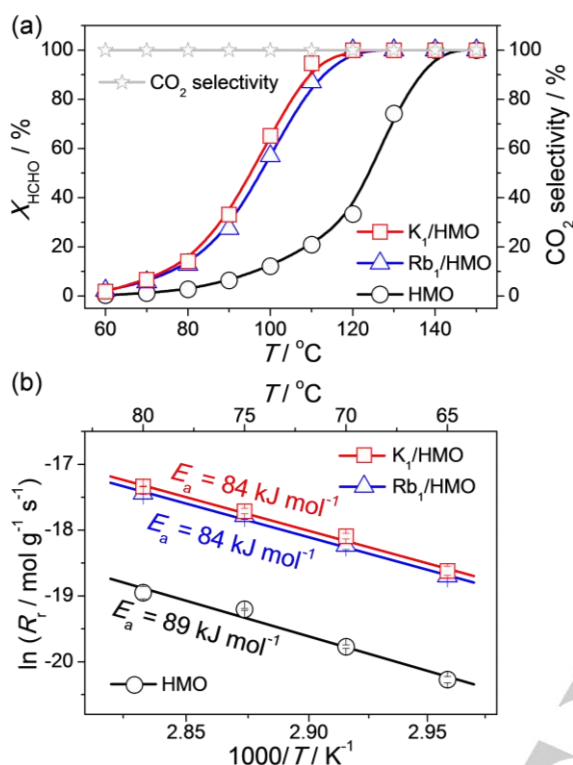


**Figure 4.** (a)  $X_{\text{HCHO}}$  and  $\text{CO}_2$  selectivity as a function of reaction temperature ( $T$ ) over  $\text{K}_1/\text{HMO}$ ,  $\text{Rb}_1/\text{HMO}$ , or HMO. (b) Arrhenius plots for the reaction rates ( $R_r$ ) with the corresponding activation energy ( $E_a$ ) of the HCHO oxidation over  $\text{K}_1/\text{HMO}$ ,  $\text{Rb}_1/\text{HMO}$ , or HMO.

The mechanism of catalytic oxidation of HCHO at low temperatures often follows the Mars-van Krevelen model,<sup>[21,37]</sup> and thus the dissociation of O<sub>2</sub> and the oxidation of adsorbed formate intermediate are considered as two critical steps.<sup>[37]</sup> To determine the rate-determining step, we studied the surface reaction kinetics of HCHO oxidation at low temperatures over HMO,  $\text{K}_1/\text{HMO}$ , and  $\text{Rb}_1/\text{HMO}$  at the  $X_{\text{HCHO}}$  less than 30%. As shown in Figure 5a, the reaction orders ( $k_r$ ) of HCHO over three samples are equal ( $k_r = -0.3$ ), indicating that the oxidation of adsorbed formate intermediate is not the rate-determining step. The  $k_r$  of O<sub>2</sub> is only 0.2 for HMO, and it dramatically increases to 0.9 for  $\text{K}_1/\text{HMO}$  and 0.8 for  $\text{Rb}_1/\text{HMO}$  (Figure 5b). Because of the negative  $k_r$  for HCHO over both HMO and the single-atom alkali catalysts, the activation of O<sub>2</sub> will be inhibited by surface adsorbed HCHO until surface lattice oxygen species are active enough to react with the adsorbed HCHO to produce CO<sub>2</sub> and H<sub>2</sub>O, concomitant with the generation of oxygen defects. The almost first-order dependence on O<sub>2</sub> concentration for the single-atom alkali catalysts implies that the HMO lattice oxygen species in contact with the single alkali ions are highly active for converting adsorbed HCHO to CO<sub>2</sub> and H<sub>2</sub>O, and that the single

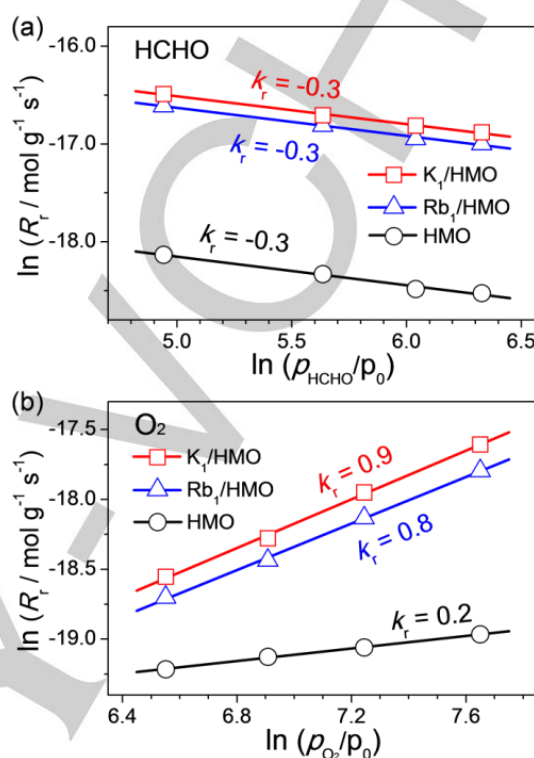


**Figure 5.** Reaction kinetics data of the catalytic oxidation of HCHO. Reaction orders ( $k_r$ ) for (a) HCHO and (b) O<sub>2</sub> at the reaction temperature of 90 °C over HMO,  $\text{K}_1/\text{HMO}$ , or  $\text{Rb}_1/\text{HMO}$ .

The oxygen activation of the catalysts is essentially associated with the nature of the active sites, and thus we used X-ray absorption spectroscopies (XAS) to investigate the electronic structures of the single alkali ions. Figure 6 shows the XANES data of  $\text{K}_1/\text{HMO}$  and  $\text{Rb}_1/\text{HMO}$  together with two references at the K and Rb  $K$ -edges. Since the  $1s \rightarrow 3d$  pre-edge features are sensitive to the coordination geometry of excited atoms,<sup>[38]</sup> the alkali ions in KCl or RbOH do not have the pre-edge absorption peaks because of the  $1s \rightarrow 3d$  dipole-forbidden transitions,<sup>[39]</sup> indicating the absence of the  $d$ - $sp$  orbital hybridization, consistent with their stable outermost electronic configurations. Particularly, the alkali ions of  $\text{K}_1/\text{HMO}$  and  $\text{Rb}_1/\text{HMO}$  with a  $D_{4h}$  symmetry have relatively intense pre-edge peaks, indicating the presence of the  $1s \rightarrow 3d$  dipole-allowed transition. The results demonstrate that the alkali ions have  $d$ - $sp$  hybridized orbitals.<sup>[38]</sup> The alkali  $d$ - $sp$  hybridizations may originate from the electron transfer from O  $sp^3$  orbitals with lone-pair electrons to unoccupied alkali  $d$ - $sp$  frontier orbitals, resulting in electron-rich alkali atoms, analogous to metallic alkali atoms with the outermost hybridized orbitals.<sup>[40]</sup>

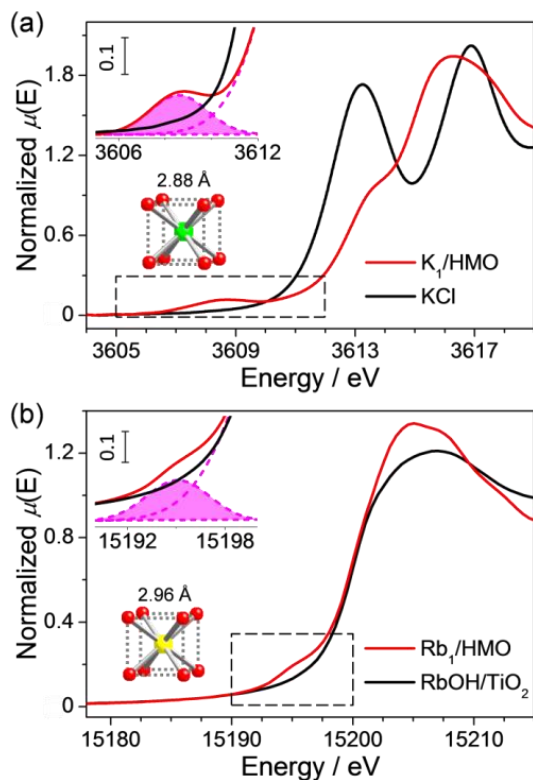


**Figure 6.** XANES spectra of (a)  $K_1/HMO$  and  $KCl$ , and (b)  $Rb_1/HMO$  and  $RbOH/TiO_2$  at the K and Rb  $K$ -edges. Insets: spectral fitting edges, the pink shadows showing the  $1s \rightarrow 3d$  transition, and models of (a)  $KO_8$  and (b)  $RbO_8$  structure motifs.

The oxidation states of the alkali atoms of the single-atom alkali catalysts were determined by using  $K 2p$  and  $Rb 3d$  XPS. The electron densities of states of single alkali adatoms are much higher than the ideal alkali ions with a normal oxidation state of +1 in  $KCl$  or  $RbOH$ . As shown in Figure 7a and according to our recent report,<sup>[23]</sup> it is reasonably deduced that the potassium atoms of  $K_1/HMO$  have the electron density of states higher than that of  $K^+$ , and the same results are also obtained from density functional theoretical (DFT) calculation shown in Figure S5. Likewise, the binding energy (BE) of the  $Rb 3d_{5/2}$  peak of  $RbOH$  is centered at 109.3 eV, characteristic of  $Rb^+$ ,<sup>[41]</sup> whereas the BE of  $Rb 3d_{5/2}$  of  $Rb_1/HMO$  decreases to  $\sim 108.2$  eV by a downshift of  $\sim 1.1$  eV with respect to that of  $RbOH$  (Figure 7b), indicative of the high electronic density of states of Rb ions. The results are in line with the above XANES data. The single alkali adatoms with the hybridized  $d$ - $sp$  orbitals and the high electronic density of states are energetically favorable for the adsorption and subsequent dissociation of  $O_2$ : (i) The orbital hybridization of single alkali adatoms by local transfer of  $sp$  electrons to empty  $d$  shell allows  $O_2$  to approach alkali atoms until chemisorption occurs because of the Pauli repulsion weakening; (ii) the abundant electrons of single alkali adatoms are favorable for charge transfer to antibonding  $\pi^*$  orbitals of  $O_2$  to weaken the O-O bond until dissociation occurs.<sup>[27]</sup> As a consequence, the high electronic density of

states of the single alkali adatoms is mainly responsible for the strong ability towards activating  $O_2$ .

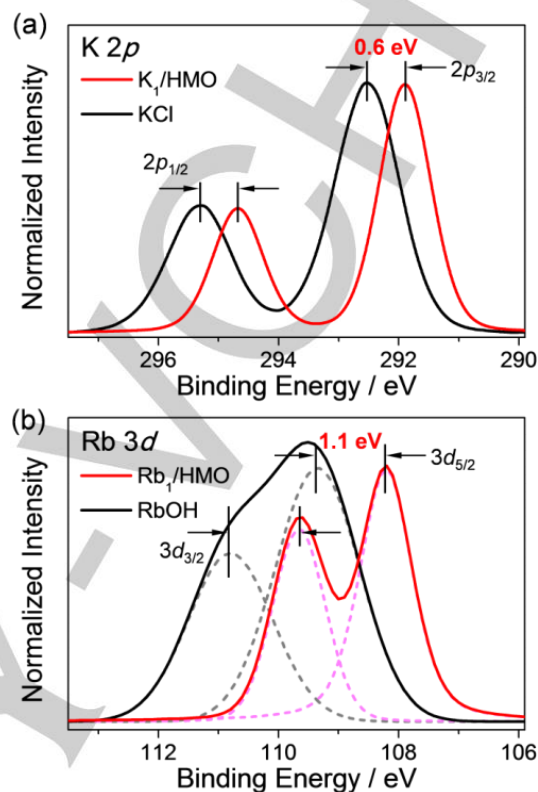


**Figure 7.** (a)  $K 2p$  XPS of  $K_1/HMO$  and  $KCl$  showing the shift of binding energy. (b)  $Rb 3d$  XPS of  $Rb_1/HMO$  and  $RbOH$  showing the shift of binding energy.

The activation of oxygen also includes the activation of lattice oxygen besides molecular  $O_2$ . Figure 8 depicts the  $O 1s$  XPS of HMO and  $K_1/HMO$  and  $Rb_1/HMO$  together with their differences. Obviously, the  $O 1s$  XPS of  $K_1/HMO$  and  $Rb_1/HMO$  slightly shifts to lower BE compared to HMO, illustrating that the O species gains electrons after the loading of alkalis on HMO. The main peak in the BE range of 529.6-529.8 eV is assigned to the surface lattice oxygen ( $O_{sl}$ ) species of HMO, and the smaller shoulder peak in a BE range of 530.9-531.3 eV is ascribed to surface defect oxygen ( $O_{sd}$ ) species of HMO.<sup>[42]</sup> In particular, the  $O_{sd}$  species decrease while the  $O_{sl}$  species increase in single-atom alkali catalysts with respect to those of HMO, implying that the concentration of the  $O_{sl}$  species of HMO increases after the loading of alkalis. On the basis of the Mars-van Krevelen model, the  $O_{sl}$  species are of great importance for low-temperature oxidation of HCHO because  $O_{sl}$  with nucleophilic property can attack the electrophilic carbonyl group of HCHO readily.<sup>[43]</sup> Therefore, the enhancement of the  $O_{sl}$  species concentration with alkali loading could partially accounts for the activity improvement of  $K_1/HMO$  and  $Rb_1/HMO$ . Therefore, according to the evidence and the related discussion, the enhancement of the single-atom alkali catalysts mainly originates from the facile

activation of molecular O<sub>2</sub> by electron-abundant alkali ions and active lattice oxygen due to the alkali loading.

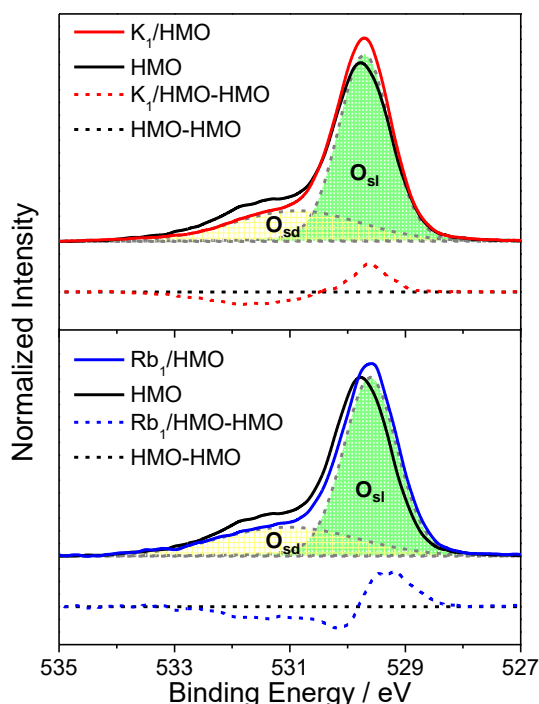


**Figure 8.** O 1s XPS of HMO and K<sub>1</sub>/HMO and Rb<sub>1</sub>/HMO together with their differences (dotted lines). The shades in different colors show curve-fitting results, and the shades in yellow and green represent O<sub>sd</sub> and O<sub>sl</sub> species, respectively.

The significant change of the catalytic performance of the inert alkali metal ions when they are loaded on HMO may essentially originate from the electronic metal-support interactions (EMSI). Thus, we obtained soft-X-ray adsorption spectra of the samples to shed light on such interactions. According to the forthcoming DFT calculations and the previous reports,<sup>[44,45]</sup> the insulating HMO will become conducting after alkalis are inserted into the tunnels. Because the electronegativity of manganese is much smaller than that of oxygen, the electrons transferred to alkalis should mainly originate from manganese. Accordingly, we studied the changes of the Mn L<sub>3</sub>-edge soft-X-ray absorption spectra of HMO after the insertion of K ions into the tunnels. The results are shown in Figure 9a.

According to the O<sub>h</sub> symmetry of Mn and the crystal field theory, two peaks in the Mn L<sub>3</sub>-edge soft-X-ray absorption spectra of HMO and K<sub>1</sub>/HMO are assigned to the 2p<sub>3/2</sub> → t<sub>2g</sub> and 2p<sub>3/2</sub> → e<sub>g</sub> transitions, and thus an energy difference between t<sub>2g</sub> and e<sub>g</sub> orbitals, a so-called octahedral ligand-field splitting parameter 10Dq, is calculated to be ~2.4 eV, consistent with the reported value.<sup>[46]</sup> In particular, the intensity of the peak due to the 2p<sub>3/2</sub> → e<sub>g</sub> transition is slightly stronger for K<sub>1</sub>/HMO than HMO, elucidating that the unoccupied states increase for K<sub>1</sub>/HMO, i.e., Mn loses part of e<sub>g</sub> electrons after the K insertion because the pristine HMO has a minority of Mn<sup>3+</sup> with 3d<sup>4</sup>

electrons in a high-spin electron configuration t<sub>2g</sub><sup>3</sup>e<sub>g</sub><sup>1</sup>.<sup>[47]</sup> Possibly, electron transfer from Mn to K via the bridging oxygen of K-O-Mn occurs when K ions are inserted into HMO tunnels.

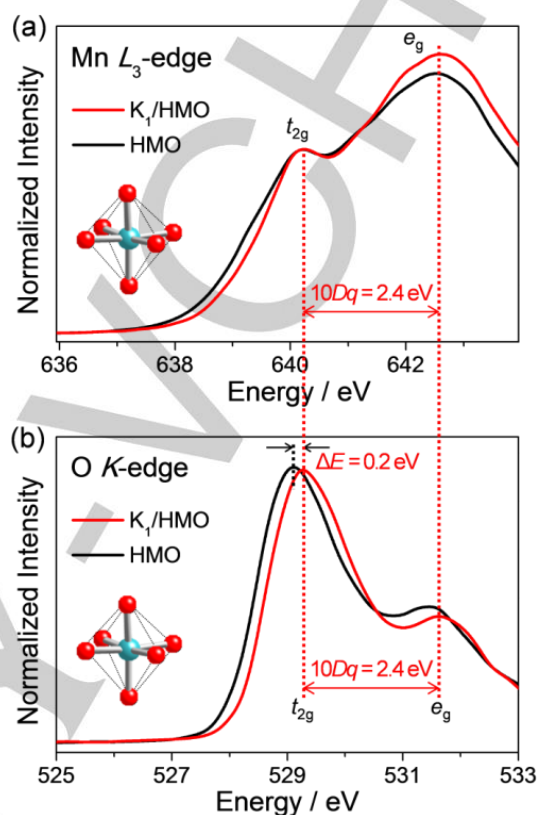


**Figure 9.** (a) Mn L<sub>3</sub>-edge and (b) O K-edge soft-X-ray absorption spectra of HMO and K<sub>1</sub>/HMO. Inset: MnO<sub>6</sub> octahedron. Red and blue balls represent O and Mn, respectively.

To substantiate the above hypothesis, we recorded the O K-edge soft-X-ray adsorption spectra of HMO and K<sub>1</sub>/HMO. As shown in Figure 9b, a distinct feature of two peaks with an energy difference of ~2.4 eV evidences that the O 2p orbitals have hybridized with the Mn 3d orbitals.<sup>[46]</sup> The high energy peak intensity of K<sub>1</sub>/HMO with the “e<sub>g</sub>” feature is slightly weaker with respect to that of HMO, indicating that the occupied states of the O 2p orbitals with the “e<sub>g</sub>” feature increase. By comparing the peak intensity due to the Mn e<sub>g</sub> orbitals with the intensity of the O 2p orbitals with the “e<sub>g</sub>” feature, we conclude that electrons on the Mn e<sub>g</sub> orbitals have transferred into the unoccupied O 2p orbitals through hybridization. Therefore, the electron transfer from manganese to alkalis through bridging oxygen allows alkalis to be at the high electronic density of states.

In Figure 9b, another important characteristic of the O K-edge soft-X-ray absorption spectra is the upshifted spectrum of K<sub>1</sub>/HMO with respect to that of HMO, indicating that electron transfer from the Mn e<sub>g</sub> orbitals to the unoccupied O 2p orbitals leads to the electronic states of O to shift up to a higher energy by 0.2 eV with comparison to that of HMO. As discussed above,

the electronic density of states of the high-energy O 2p orbitals with the “e<sub>g</sub>” feature increases due to the insertion of K<sup>+</sup> into HMO tunnels. Hence, the upshifted O 2p orbitals with the high electronic density of states should improve the redox ability of the single-atom alkali catalysts, which possibly accounts for the production of the highly active lattice oxygen after loading alkalis.

Figure 10 shows the H<sub>2</sub> temperature-programmed reduction (H<sub>2</sub>-TPR) profiles of HMO and K<sub>1</sub>/HMO. As Figure 10a shows, HMO exhibits three reduction peaks. The first and second peaks are located at ~269 and 279 °C, respectively, while the third weak broad peak starts at 300 °C with a maximum at ~445 °C. The area ratio of H<sub>2</sub> consumption ( $A_{H_2}$ ) between the sum of former two peaks and the third peak is ~1.6:1, from which the oxidation state of Mn can be calculated to be ~3.7, indicating the presence of Mn<sup>3+</sup> and Mn<sup>4+</sup>, and thus the formula of HMO can be simplified to be MnO<sub>1.9</sub>. The first peak is due to the reduction of the surface oxygen (O<sub>sd</sub> and O<sub>sl</sub>) species. The second and third peaks can be assigned to the reduction of the bulk lattice oxygen (O<sub>bl</sub>) species, i.e., the reduction of MnO<sub>1.9</sub> to Mn<sub>3</sub>O<sub>4</sub>, and the reduction of Mn<sub>3</sub>O<sub>4</sub> to MnO.<sup>[16]</sup> After alkali loading, two typical features of the H<sub>2</sub>-TPR profile of K<sub>1</sub>/HMO can be observed: (i) the surface O species increase, (ii) the temperature required for the reduction of the O<sub>bl</sub> species shifts down to the low-temperature window.

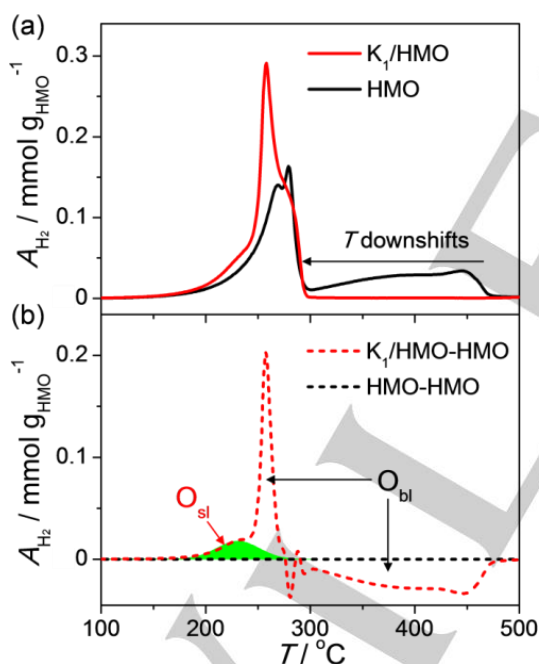


**Figure 10.** (a) H<sub>2</sub>-TPR profiles of HMO and K<sub>1</sub>/HMO, and (b) the difference curves by subtracting the H<sub>2</sub>-TPR curve of HMO. The green shade in panel (b) represents the H<sub>2</sub> consumption by active O<sub>sl</sub> at the vicinity of alkali ions.

To shed light on the discrepancy after the alkali loading, the difference curves are obtained by subtracting the H<sub>2</sub>-TPR curve of HMO, as shown in Figure 10b, and thus a peak centered at ~230 °C can be attributed to the reduction of O<sub>sl</sub> at the vicinity of

alkali ions, indicating that the number of the active O<sub>sl</sub> increases and the redox ability is improved, consistent with the upshift in energy of O K-edge soft-X-ray absorption spectra of K<sub>1</sub>/HMO in Figure 9b. Moreover, the abundance of active O<sub>sl</sub> species is also favorable for improving the catalytic activity in HCHO oxidation. Note that after alkali loading, the high-temperature reduction peak of HMO drastically shifts down to the low temperature range, and the peaks due to the reduction of O<sub>sl</sub> are in a narrow temperature window, implying that the alkali loading accelerates the transfer rates of electrons produced in the redox reaction of H<sub>2</sub> with O<sub>bl</sub>. Therefore, the electron transfer between alkalis and HMO enhances the redox ability, thus leading to the high catalytic activity of the single-atom alkali catalysts in HCHO oxidation.

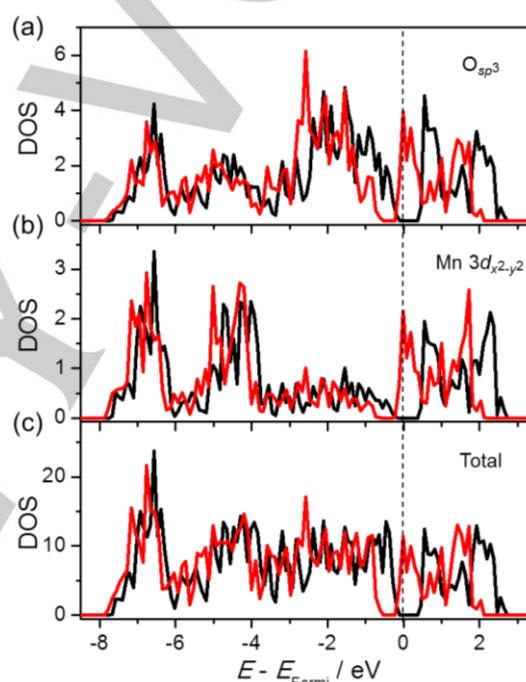


**Figure 11.** DOS of the (a) O<sub>sp3</sub> and (b) Mn 3d<sub>x<sup>2</sup>-y<sup>2</sup></sub> of HMO (black) and K<sub>1</sub>/HMO (red). (c) Total DOS of HMO (black) and K<sub>1</sub>/HMO (red).

To investigate the EMSI in detail, we carried out DFT calculations based on HMO and K<sub>1</sub>/HMO. Figure 11a,b depicts the electronic densities of states (DOS) of HMO and K<sub>1</sub>/HMO. The DOS of the O<sub>sp3</sub> orbital bound to K<sup>+</sup> shifts downward in energy with respect to that of HMO, making the DOS of Mn 3d<sub>x<sup>2</sup>-y<sup>2</sup></sub> orbitals shift down below the Fermi level ( $E_{Fermi}$ ). The DOS downshifts of both O and Mn demonstrate that the strong EMSI occurs along the K-O-Mn structural motif. These results agree fairly with the soft-X-ray absorption spectroscopy results in Figure 9, which proved electron transfer from Mn to K via the bridging O. Figure 11c shows the total DOS of HMO and K<sub>1</sub>/HMO. Interestingly, the EMSI induces an insulator-to-conductor transition (HMO is insulating, but K<sub>1</sub>/HMO is conducting), which is favorable for facilitating electron transfer in

catalytic reactions, thus leading to the enhancement of redox ability (Figure 10) and catalytic activity (Figure 4).<sup>[27]</sup> Likewise, alkali earth metal ions such as  $\text{Ca}^{2+}$  were proved to be able to improve the oxidizing ability of manganese-oxido clusters<sup>[48]</sup> or iron-oxo complexes<sup>[49]</sup> by accelerating electron transfer in oxidation reactions. Therefore, the EMSI allows the DOS of the alkali ions to increase by the electron transfer from Mn to K, which improves the activation of  $\text{O}_2$  and lattice oxygen, thus leading to the high catalytic activity in HCHO oxidation.

## Conclusions

In summary, single-atom alkali catalysts were synthesized by anchoring individual alkali atoms on the tunnel openings of HMO. The structures were precisely determined by using SXRD, X-ray absorption, and TEM. These single-atom alkali catalysts exhibited high catalytic activity in the complete oxidation of HCHO in the presence of  $\text{O}_2$  at low temperatures. The characterization results demonstrated that the single alkali atoms have the frontier  $d$ - $sp$  hybridized orbitals via the strong interaction with lattice oxygen, and that the electron transfer from the Mn  $e_g$  orbitals to the alkali  $d$ - $sp$  hybridized orbitals through the alkali-O-Mn bridging O makes alkali atoms have high electronic density of states. Hence, the electron-rich alkali atoms with hybridized orbitals can facilitate the sticking and activation of  $\text{O}_2$ . The combination of O  $K$ -edge soft-X-ray absorption spectra and  $\text{H}_2$ -TPR profiles elucidated that the electronic states of the single-atom alkali catalysts shift up in energy, so that the lattice oxygen shows strong redox ability. Therefore, the high electron density of states of the single alkali atoms and the high activity of lattice oxygen are responsible for the high catalytic activity of the single-atom alkali catalysts in HCHO oxidation.

## Experimental Section

### Catalyst preparation

HMO was prepared by a refluxing route:<sup>[32]</sup>  $\text{MnSO}_4 \cdot \text{H}_2\text{O}$  (25.350 g, 0.15 mol),  $(\text{NH}_4)_2\text{S}_2\text{O}_8$  (34.200 g, 0.15 mol) and  $(\text{NH}_4)_2\text{SO}_4$  (99.000 g, 0.75 mol) were dissolved in deionized water (0.4 L) to give an aqueous solution. Then the solution was heated and kept at 100 °C for 12 h under refluxing. The resulting slurry was filtered, washed with deionized water, dried at 110 °C for 12h and the obtained black solid was calcined in air at 400 °C for 4h.

Single-atom alkali catalysts were prepared by an impregnation method. In a typical synthesis, KCl (0.216 g, 2.9 mmol) or RbOH (0.297 g, 2.9 mmol) was added to a suspension (50 mL) containing HMO (2.000 g, 23.0 mmol) with vigorously stirring for 15 min. Then the suspension was transferred to a rotary evaporator and kept the temperature at 80 °C to remove the excess water. The obtained dry samples were labeled as KCl/HMO and RbOH/HMO, respectively.  $\text{A}_x/\text{HMO}$  ( $\text{A} = \text{K}$  or  $\text{Rb}$ ) sample was obtained after annealing KCl/HMO or RbOH/HMO at 400 °C for 12 h and the final powder was washed by deionized water at room temperature. The alkali loadings (4.8 wt.% for  $\text{K}_1/\text{HMO}$  and 10.4 wt.% for  $\text{Rb}_1/\text{HMO}$ ) were determined by using XRF on a Bruker-AXS S4 Explorer. For comparison, RbOH/ $\text{TiO}_2$  was also prepared by impregnation of  $\text{TiO}_2$

(2.000 g, 25.0 mmol) with RbOH (0.297 g, 2.9 mmol) and without further annealing.

### Catalyst characterizations

The SXRD were performed at BL14B of the Shanghai Synchrotron Radiation Facility (SSRF) at a wavelength of 0.6887 Å. Rietveld refinements of the diffraction data were performed with the FULLPROF software package on the basis of the space group  $I4/m$ .

The specific surface area and pore volume were analyzed on a Micromeritics Tristar II 3020 surface area and pore size analyzer by  $\text{N}_2$  adsorption-desorption measurements at -196 °C, and calculated by the Brunauer-Emmett-Teller (BET) and the  $t$ -plot method, respectively.

The XAS of the  $\text{K}_1/\text{HMO}$  including the XANES spectra and EXAFS spectra at the K  $K$ -edge were collected at BL4B7A of the Beijing Synchrotron Radiation Facility (BSRF). The Rb  $K$ -edge XANES and EXAFS spectra were collected at BL14W of the SSRF. The raw data were analyzed using the IFEFFIT 1.2.11 software package. The soft-X-ray absorption spectra at the Mn  $L$ -edge and O  $K$ -edge were obtained in a total electron yield (TEY) mode at BL08U1A of the SSRF.

TEM and HRTEM images were obtained on a JEM 2100F transmission electron microscope with EDX for determination of elemental contents.

The XPS was obtained on Kratos Axis Ultra-DLD system with a charge neutralizer and a 150 W Al (Mono) X-ray gun (1486.6 eV). The samples were dried in vacuum before XPS analysis. The XPS were referenced to the C 1s peak at the BE of 284.6 eV. Data analysis and processing were undertaken using XPSpeak 4.1 with the Shirley type background.

The  $\text{H}_2$ -TPR profiles were measured by a thermal conductivity detector (TCD) on a Micromeritics 2720 adsorption instrument (Micromeritics, USA). A sample (50 mg) was loaded and reduced by 10.0 vol.%  $\text{H}_2/\text{Ar}$  (50 mL  $\text{min}^{-1}$ ) at a heating rate of 10 °C  $\text{min}^{-1}$ . The  $\text{A}_{\text{H}_2}$  was calculated and calibrated by pure CuO samples.

### Catalytic evaluations

The catalytic oxidation of HCHO was conducted in a fixed-bed quartz reactor (inner diameter = 8 mm) at atmospheric pressure. A fresh catalyst (50 mg, 40–60 mesh) was loaded for each run. Gaseous HCHO was generated by passing  $\text{N}_2$  over paraformaldehyde (96%, Acros) in a container, which was immersed in a water bath to keep the temperature at 45 °C. The HCHO/ $\text{N}_2$  gas was mixed with another  $\text{O}_2$  flow to give a total gas stream of 140 ppm HCHO/10.0 vol.%  $\text{O}_2/\text{N}_2$  (100 mL  $\text{min}^{-1}$ ). The gas hourly space velocity is 60,000  $\text{h}^{-1}$ . The gas analysis was undertaken using an on-line Agilent 7890A gas chromatograph equipped with a TCD. The  $\text{CO}_2$  selectivity was correctly measured by using an on-line Agilent 7890B gas chromatograph equipped with FID and Ni catalyst converter, which could convert carbon oxides quantitatively into methane in the presence of  $\text{H}_2$  before the detector. No other carbon-containing compounds except  $\text{CO}_2$  were detected in the effluents for the whole tested temperature window and all tested catalysts. The kinetics of HCHO oxidation was studied at 90 °C over  $\text{K}_1/\text{HMO}$ ,  $\text{Rb}_1/\text{HMO}$ , and HMO at the  $X_{\text{HCHO}}$  less than 30% to achieve the data of the intrinsic reaction kinetics by excluding the external and internal diffusion. The HCHO concentration ranged from 140 to 560 ppm, and the corresponding  $\text{O}_2$  concentration ranged from 700 to 2100 ppm. In typical runs, the data were recorded at the steady state.

### Theoretical calculations

All of the features were based on the density functional theory as implemented in the Vienna Ab-initio Simulation Package (VASP). The Local Density Approximation (LDA) for the exchange and correlation effects was used in the calculations. To describe the interactions

between the core and valence electrons, the pseudo potentials of projector augmented wave method were used. The plane wave energy was equal to 500 eV, and a  $2 \times 2 \times 6$  monkhorst-pack grid was used for k-space sampling in the calculation of HMO or K<sub>1</sub>/HMO. For the geometry optimization, the force and energy cutoff were set as 0.01 eV/Å and  $10^{-6}$  eV. The lattice constants and wyckoff sites informations for a conventional tetragonal cell were listed in the Table S1 and S2. A supercell containing 8 formula units of MnO<sub>2</sub> was employed in the calculations for K<sup>+</sup> in the terminal the tunnels. For the DOS calculation of the system, we have used LDA with Hubbard U corrections (LDA+U) method, and the U and J values were set as 5.6 eV and 1.0 eV, respectively.<sup>[50,51]</sup>

## Acknowledgements

This work was financially supported by the NSFC (21477023 and 21777030). The SXRD and XAS measurements were conducted at the SSRF and BSRF, Chinese Academy of Sciences.

**Keywords:** single-atom alkali catalysts • heterogeneous catalysis • structure elucidation • electron transfer • oxygen activation

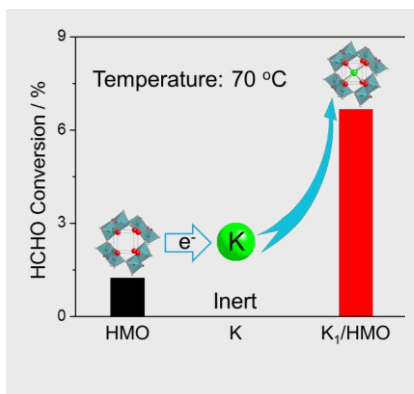
- [1] X. Tang, Y. Bai, A. Duong, M. T. Smith, L. Li, L. Zhang, *Environ. Int.* **2009**, *35*, 1210–1224.
- [2] O. Wittmann, *Eur. J. Wood Wood Prod.* **1962**, *20*, 221–224.
- [3] WHO Guidelines for Indoor Air Quality: Selected Pollutants, World Health Organization Regional Office for Europe, Copenhagen, Denmark, **2010**.
- [4] W. D. Kerns, K. L. Pavkov, D. J. Donofrio, E. J. Gralla, J. A. Swenberg, *Cancer Res.* **1983**, *43*, 4382–4392.
- [5] J. A. Swenberg, W. D. Kerns, R. I. Mitchell, E. J. Gralla, K. L. Pavkov, *Cancer Res.* **1980**, *40*, 3398–3402.
- [6] *Integrated Risk Information System (IRIS): Formaldehyde*, U.S. Environmental Protection Agency, **2006**.
- [7] T. Salthammer, *Angew. Chem. Int. Ed.* **2013**, *52*, 3320–3327.
- [8] Y. Kuwabara, G. V. Alexeeff, R. Broadwin, A. G. Salmon, *Environ. Health Persp.* **2007**, *115*, 1609–1616.
- [9] J. P. Pinto, G. R. Gladstone, Y. L. Yung, *Science* **1980**, *210*, 183–184.
- [10] J. Q. Torres, S. Royer, J. P. Bellat, J. M. Giraudon, J. F. Lamonier, *ChemSusChem* **2013**, *6*, 578–592.
- [11] X. Tang, J. Chen, X. Huang, Y. Xu, W. Shen, *Appl. Catal. B: Environ.* **2008**, *81*, 115–121.
- [12] L. Ma, D. Wang, J. Li, B. Bai, L. Fu, Y. Li, *Appl. Catal. B: Environ.* **2014**, *148–149*, 36–43.
- [13] D. W. Kwon, P. W. Seo, G. J. Kim, S. C. Hong, *Appl. Catal. B: Environ.* **2015**, *163*, 436–443.
- [14] J. Wang, J. Li, C. Jiang, P. Zhou, P. Zhang, J. Yu, *Appl. Catal. B: Environ.* **2017**, *204*, 147–155.
- [15] J. Zhou, L. Qin, W. Xiao, C. Zeng, N. Li, T. Lv, H. Zhu, *Appl. Catal. B: Environ.* **2017**, *207*, 233–243.
- [16] T. Chen, H. Dou, X. Li, X. Tang, J. Li, J. Hao, *Micropor. Mesopor. Mater.* **2009**, *122*, 270–274.
- [17] S. Liang, F. Teng, G. Bulgan, R. Zong, Y. Zhu, *J. Phys. Chem. C* **2008**, *112*, 5307–5315.
- [18] X. Yu, J. He, D. Wang, Y. Hu, H. Tian, Z. He, *J. Phys. Chem. C* **2012**, *116*, 851–860.
- [19] X. Yu, J. He, D. Wang, Y. Hu, H. Tian, T. Dong, Z. He, *J. Nanopart. Res.* **2012**, *14*, 1–14.
- [20] H. Tian, J. He, L. Liu, D. Wang, *Ceram. Int.* **2013**, *39*, 315–321.
- [21] Z. Huang, X. Gu, Q. Cao, P. Hu, J. Hao, J. Li, X. Tang, *Angew. Chem. Int. Ed.* **2012**, *51*, 4198–4203.
- [22] P. Hu, Z. Amghouz, Z. Huang, F. Xu, Y. Chen, X. Tang, *Environ. Sci. Technol.* **2015**, *49*, 2384–2390.
- [23] F. Xu, Z. Huang, P. Hu, Y. Chen, L. Zheng, J. Gao, X. Tang, *Chem. Commun.* **2015**, *51*, 9888–9891.
- [24] J. Xu, T. White, P. Li, C. He, Y. F. Han, *J. Am. Chem. Soc.* **2010**, *132*, 13172–13173.
- [25] D. J. Dwyer, J. H. Hardenbergh, *Appl. Surf. Sci.* **1984**, *19*, 14–27.
- [26] G. Ertl, M. Weiss, S. B. Lee, *Chem. Phys. Lett.* **1979**, *60*, 391–394.
- [27] C. Janiak, R. Hoffmann, P. Sjövall, B. Kasemo, *Langmuir* **1993**, *9*, 3427–3440.
- [28] J. Harris, S. Andersson, *Phys. Rev. Lett.* **1985**, *55*, 1583–1586.
- [29] J. E. Post, R. B. Von Dreele, P. R. Buseck, *Acta Cryst., B* **1982**, *38*, 1056–1065.
- [30] R. D. Shannon, C. T. Prewitt, *Acta Cryst., B* **1969**, *25*, 925–946.
- [31] J. Vicat, E. Fanchon, P. Strobel, D. Tran Qui, *Acta Cryst., B* **1986**, *42*, 162–167.
- [32] P. Hu, M. E. Schuster, Z. Huang, F. Xu, S. Jin, Y. Chen, W. Hua, D. S. Su, X. Tang, *Chem. Eur. J.* **2015**, *21*, 9619–9623.
- [33] J. Vogt, H. Weiss, *Surf. Sci.* **2001**, *491*, 155–168.
- [34] S. Odde, H. M. Lee, M. Kolaski, B. J. Mhin, K. S. Kim, *J. Chem. Phys.* **2004**, *121*, 4665–4670.
- [35] Q. Li, X. Wang, Y. Xin, Z. Zhang, Y. Zhang, C. Hao, M. Meng, L. Zheng, L. Zheng, *Sci. Rep.* **2014**, *4*, 4725.
- [36] Y. Chen, G. Tian, M. Zhou, Z. Huang, C. Lu, P. Hu, J. Gao, Z. Zhang, X. Tang, *Environ. Sci. Technol.* **2016**, *50*, 5825–5831.
- [37] C. F. Mao, M. A. Vannice, *J. Catal.* **1995**, *154*, 230–244.
- [38] S. Bordiga, E. Groppo, G. Agostini, J. A. van Bokhoven, C. Lamberti, *Chem. Rev.* **2013**, *113*, 1736–1850.
- [39] L. G. Parratt, *Rev. Mod. Phys.* **1959**, *31*, 616–645.
- [40] L. Pauling, *General Chemistry*, BN Publishing, **2011**.
- [41] R. Itti, I. Tomeno, K. Ikeda, K. Tai, N. Koshizuka, S. Tanaka, *Phys. Rev. B* **1991**, *43*, 435–440.
- [42] Q. Tang, L. Jiang, J. Liu, S. Wang, G. Sun, *ACS Catal.* **2014**, *4*, 457–463.
- [43] X. Tang, J. Chen, Y. Li, Y. Xu, W. Shen, *Chem. Eng. J.* **2006**, *118*, 119–125.
- [44] M. Toupin, T. Brousse, D. Bélanger, *Chem. Mater.* **2004**, *16*, 3184–3190.
- [45] W. Xiao, H. Xia, J. Y. Fuh, L. Lu, *J. Power Sources* **2009**, *193*, 935–938.
- [46] M. Abbate, F. M. F. de Groot, J. C. Fuggle, A. Fujimori, O. Strebler, F. Lopez, M. Domke, G. Kaindl, G. A. Sawatzky, M. Takano, Y. Takeda, H. Eisaki, S. Uchida, *Phys. Rev. B* **1992**, *46*, 4511–4519.
- [47] P. Umek, A. Gloter, M. Pregelj, R. Dominko, M. Jagličić, Z. Jagličić, A. Zimina, M. Brzhezinskaya, A. Potočnik, C. Filipič, A. Levstik, D. Arčon, *J. Phys. Chem. C* **2009**, *113*, 14798–14803.
- [48] E. Y. Tsui, R. Tran, J. Yano, T. Agapie, *Nature Chem.* **2013**, *5*, 293–299.
- [49] Y. Morimoto, H. Kotani, J. Park, Y. Lee, W. Nam, S. Fukuzumi, *J. Am. Chem. Soc.* **2011**, *133*, 403–405.
- [50] F. Zhou, M. Cococcioni, C. A. Marianetti, D. Morgan, G. Ceder, *Phys. Rev. B* **2004**, *70*, 235121.
- [51] D. A. Tompsett, M. S. Islam, *Chem. Mater.* **2013**, *25*, 2515–2526.

## Entry for the Table of Contents (Please choose one layout)

Layout 1:

## FULL PAPER

Inert alkali metal ions were successfully activated in completely oxidation of HCHO at low temperatures by electron transfer from Mn to K via the bridging oxygen of K-O-Mn when anchored onto hollandite manganese oxide surfaces.



Jiayi Gao, Zhiwei Huang, Yaxin Chen, Jing Wan, Xiao Gu, Zhen Ma, Jianmin Chen, Xingfu Tang\*

Page No. 1 – Page No. 9

Activating Inert Alkali Metal Ions by Electron Transfer from Manganese Oxide for Formaldehyde Abatement

Layout 2:

## FULL PAPER

((Insert TOC Graphic here; max. width: 11.5 cm; max. height: 2.5 cm))

Author(s), Corresponding Author(s)\*

Page No. – Page No.

Title

Text for Table of Contents